

Experimental validation of a fast control-oriented, physics-informed surrogate model for plasma equilibrium reconstruction in the TCV tokamak

M. Grandin¹, A. Mele², C. Galperti², D. Gonzales Castineiras², C. Heiß², A. Cenedese¹,
TCV team³ and EUROfusion Tokamak Exploitation team⁴

Abstract—Magnetic equilibrium reconstruction provides the plasma state estimate required for real-time shape control in tokamaks. We present a fast, physics-informed neural network surrogate of the `liuqe` equilibrium reconstruction code [1] for the TCV tokamak at EPFL, achieving inference times below 100 μ s and enabling 10 kHz shape control.

The model is trained on around 10,000 TCV discharges spanning the full operational range of plasma shapes. Its modular branch/trunk architecture decouples magnetic measurement encoding from spatial coordinate processing, enabling physics-informed regularization via automatic differentiation of the predicted flux map.

The surrogate has been compiled and deployed on the TCV real-time control system, and validated both offline and in real time against the models `liuqe-rt` and `lih`, showing comparable accuracy. Closed-loop performance assessed with the real-time software in-the-loop `fgc` [2] demonstrates control-equivalent behavior across multiple control strategies.

I. INTRODUCTION

Plasma shape control is a central challenge in tokamak operation, as the plasma boundary determines interactions with plasma-facing components, MHD stability margins, and confinement performance. High control bandwidth is particularly important for advanced or inherently unstable plasma configurations, during fast current ramp-up and ramp-down transients, and more generally to improve shape-tracking accuracy. A 10 kHz shape-control loop would be desirable on these grounds alone; it would additionally enable the unification of shape control with vertical position stabilization, which on most tokamaks already runs at high bandwidth.

The Tokamak à Configuration Variable (TCV) at EPFL is designed to explore a wide range of plasma shapes and control strategies [3], being equipped with poloidal field (PF) coils and magnetic diagnostics (flux loops and field probes) around the vacuum vessel. The standard equilibrium reconstruction code is `LIUQE` [1], which solves the Grad–Shafranov equation (GSE) iteratively on a 28×65 grid. `LIUQE-RT` limits iterations and interpolation complexity, achieving cycle times of ~ 0.5 ms and sustaining the current 1 kHz shape-control loop; the vertical stabilization loop, by contrast, already runs at 10 kHz. `LIH`, the zeroth-iteration first guess of the algorithm, operates at 10 kHz but with substantially reduced accuracy. The 1 kHz constraint

imposed by `LIUQE-RT` is therefore the primary bottleneck preventing both higher-bandwidth shape control and unified shape-and-position control on TCV.

The underlying physical problem is the GSE [4], [5], describing axisymmetric MHD force balance. It is useful to distinguish three related but distinct GSE-constrained problems that appear in the literature. The *free-boundary* problem takes the currents in the PF coils and passive conductors as inputs and finds the flux map together with the plasma boundary. The *fixed-boundary* problem takes a prescribed last-closed flux surface (LCFS) as a constraint and finds the PF coil currents required to sustain it. *Equilibrium reconstruction* — the problem addressed in this paper — is an inverse problem: given a set of experimental measurements (magnetic flux loops and field probes around the vacuum vessel), it seeks the flux map $\psi(r, z)$ and the two free functions $p'(\psi)$ and $TT'(\psi)$ that simultaneously satisfy the GSE and best reproduce those measurements in a least-squares sense. In general, solving the inverse problem is computationally expensive and time-consuming, thereby motivating the development of fast and parsimonious surrogate models.

Neural networks (NN) surrogates for plasma equilibrium have attracted broad interest, spanning equilibrium reconstruction [6]–[14], free-boundary equilibrium [15], and boundary and LCFS reconstruction [16]–[18], with many adopting a GSE-related physics-informed loss [8], [16], [19]–[21]. A distinct subset uses Neural Operators [22], which learn function-space mappings by separating input-function encoding from spatial coordinate processing [23], naturally yielding Physics-Informed Neural Operators (PINOs) via automatic differentiation. Recent works have applied PINO-type architectures directly to the GSE [24]–[26], including in the fixed-boundary setting [24].

On the control side, the use of a fast NN as a shape-control observer was pioneered by Bishop et al. [27] ($< 50 \mu$ s with mixed digital–analog hardware) and Jeon et al. [28], and more recently demonstrated on Globus-M/M2 [29] — albeit with a simple architecture and validated only in simulation. Data-driven approaches via Reinforcement Learning (RL) have also been applied to plasma shape control on TCV [30], DIII-D [31], and HL-3 [32]. FPGA-based acceleration has also been proposed for extreme inference latencies [33], but falls outside the scope of this work, which targets a standard single-core CPU.

In this paper, we present a PINO based on a modified DeepONet architecture [22] as a fast surrogate for `LIUQE`

¹University of Padova, Padova, Italy

²Ecole Polytechnique Federale de Lausanne (EPFL), Swiss Plasma Center (SPC), 1015 Lausanne, Switzerland

³See author list of B.P. Duval et al 2024 *Nucl. Fusion* 64 112023

⁴See author list of E. Joffrin et al 2024 *Nucl. Fusion* 64 112019

equilibrium reconstruction on TCV, in which a branch network conditioned on the magnetic measurements modulates the spatial basis functions learned by a trunk network. Physics-informed regularization is enforced via automatic differentiation through the trunk path, yielding losses on ψ , B_r , B_z , and j with LIUQE-generated targets. The model has been compiled and deployed on the TCV PCS, where it is validated in real time against LIUQE-RT and LIH. Closed-loop performance is assessed in simulation with the FGE solver [2] on a variety of control strategies.

Our work makes the following distinct contributions with respect to the existing literature. First, it demonstrates, to our knowledge, the first PINO-based equilibrium reconstruction surrogate operating at 10 kHz and deployed on the Plasma Control System (PCS) of an actual tokamak. Second, the modular branch/trunk architecture allows the learned flux map to be evaluated at arbitrary collocation points, making the approach compatible with a variety of control strategies without retraining.

The remainder of the paper is organized as follows. Section II describes the model architecture and PCS deployment; Section III presents validation and simulation results; Section IV draws conclusions.

II. METHODS

A. Grad–Shafranov Eq. and Equilibrium Reconstruction

The equilibrium of an axisymmetric magnetized plasma is governed by the GSE equation [4], [5], which expresses the balance between plasma pressure gradients and Lorentz forces in the poloidal plane (r, z) :

$$\Delta^* \psi = -4\pi^2 \mu_0 r \left(r p' + \frac{TT'}{\mu_0 r} \right), \quad (1)$$

where $\psi(r, z)$ is the poloidal magnetic flux normalized by 2π , $p'(\psi) = dp/d\psi$ and $TT'(\psi) = T dT/d\psi$ are the two free radial profile functions encoding the pressure gradient and the poloidal current function gradient respectively, and Δ^* is the Grad–Shafranov elliptic operator:

$$\Delta^* = r \frac{\partial}{\partial r} \left(\frac{1}{r} \frac{\partial}{\partial r} \right) + \frac{\partial^2}{\partial z^2}. \quad (2)$$

The poloidal magnetic field components $B_r(r, z)$ and $B_z(r, z)$ and the toroidal plasma current density $j(r, z)$ are related to ψ through its first and second partial derivatives (using standard approximations):

$$B_r(r, z) = -\frac{1}{2\pi r} \frac{\partial \psi}{\partial z}, \quad B_z(r, z) = \frac{1}{2\pi r} \frac{\partial \psi}{\partial r}, \quad (3)$$

$$j(r, z) = -\frac{1}{2\pi r} \left[\frac{\partial^2 \psi}{\partial r^2} + \frac{\partial^2 \psi}{\partial z^2} \right] + \frac{1}{2\pi r^2} \frac{\partial \psi}{\partial r}. \quad (4)$$

On TCV, LIUQE [1] parametrizes the plasma current density as a linear combination of basis functions and iteratively converges to the equilibrium on the spatial grid. LIUQE-RT limits the number of iterations per time step and adopts simplified interpolation routines, achieving $\sim 200 \mu\text{s}$ per execution. LIH corresponds to the zeroth iteration of this scheme: it fits a coarse finite-element representation of the

toroidal current distribution to the available measurements and reconstructs the flux maps via precomputed Green’s functions, operating at 10 kHz but with significantly reduced accuracy.

B. Dataset Generation

The training and validation dataset is generated by applying LIUQE [1] to all available TCV shots acquired between December 2022 and November 2025. Shots and individual time steps are filtered using basic thresholds on plasma current and on the numerical convergence of the iterative scheme, retaining only well-converged equilibria. One timestamp in every six is retained to reduce computational cost while preserving temporal variability; the resulting dataset covers approximately 10 000 shots with a broad coverage of operating conditions.

The resulting dataset spans a wide variety of plasma configurations, including limiter and diverted plasmas, standard single-null configurations (ITER-Baseline-like scenarios, the most frequent), negative and positive triangularity shapes, double-null and snowflake divertors, highly elongated plasmas, and shapes associated with plasma ramp-up and ramp-down transients. As TCV has a significantly elongated chamber, a substantial range of plasma vertical positions is also represented. The shape distribution is not uniform: single-null scenarios predominate, reflecting the operational history of the machine, but all other configurations are sufficiently represented to support generalization.

For each retained time step, the following quantities are saved: the magnetic measurements (provided by flux loops and magnetic field probes), the full poloidal flux map $\psi(r, z)$ on the computational grid, the corresponding magnetic field maps $B_r(r, z)$ and $B_z(r, z)$, and the toroidal current density map $j(r, z)$. The dataset is split at the shot level, assigning 80% of shots to the training set and 20% to the validation set. This ensures that the validation set contains only shots not seen during training, providing an unbiased estimate of generalization performance.

C. Network Architecture and Training Strategy

1) *Neural Operator Foundation*: The network architecture is grounded in the DeepONet framework introduced by Lu et al. [22], which targets the learning of mappings between functional spaces, an approach referred to as operator learning. The underlying theoretical foundation is the Universal Approximation Theorem for operators [23], which states that any nonlinear continuous operator $G : \mathbb{R}^m \rightarrow \mathbb{R}^n$ mapping an input function $u(\mathbf{x})$, sampled at locations $\mathbf{x} \in \mathbb{R}^m$, to output values at query points $\mathbf{y} \in \mathbb{R}^n$, can be approximated as

$$G(u)(\mathbf{y}) \approx \sum_{k=1}^K b_k(u(\mathbf{x})) t_k(\mathbf{y}), \quad (5)$$

where $b(\cdot)$ and $t(\cdot)$ are the *branch* and *trunk* networks respectively, and K is the number of latent units. Because \mathbf{x} and \mathbf{y} are treated independently, the model can be trained

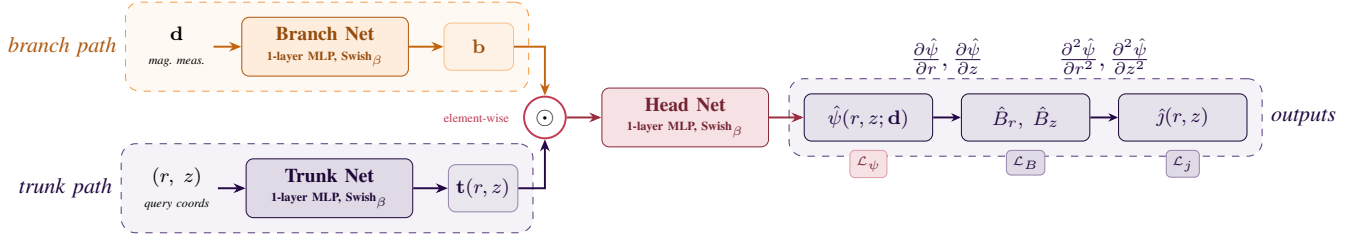


Fig. 1. Schematic of the proposed PINO architecture. The branch network encodes the vector of magnetic measurements \mathbf{d} into a latent embedding $\mathbf{b} \in \mathbb{R}^K$. The trunk network encodes the query coordinates $(r, z) \in \mathbb{R}^K$. The two embeddings are combined via element-wise multiplication and passed to a shallow regression head that produces the predicted poloidal flux $\hat{\psi}(r, z; \mathbf{d})$. Magnetic field components \hat{B}_r and \hat{B}_z are obtained via automatic differentiation through the trunk path.

and evaluated at arbitrary query points, improving flexibility and generalization capability.

Some prior works have applied Neural Operator or PINN-type architectures to GSE-related problems. Refs. [21], [24] use a DeepONet structure in which position encoding is performed on a regular grid and partial derivatives required for the physics-informed loss are estimated via finite differences. Refs. [25], [26] instead use point collocation and compute derivatives directly via automatic differentiation, but are limited either to a single fixed equilibrium or to a small set of parameter variations, and restrict collocation points to the interior of the plasma boundary. The present approach retains the branch/trunk decomposition and automatic differentiation for derivatives, while conditioning the solution on the full vector of magnetic measurements and using LIUQE-generated targets — which allows collocation points both inside and outside the LCFS.

2) *Architecture*: The network consists of three sub-networks, as illustrated in Fig. 1.

The *branch network* encodes the vector of magnetic measurements $\mathbf{d} \in \mathbb{R}^{133}$ into a latent representation:

$$\mathbf{b} = \text{BranchNet}(\mathbf{d}) \in \mathbb{R}^K. \quad (6)$$

The *trunk network* encodes the spatial query point (r, z) :

$$\mathbf{t}(r, z) = \text{TrunkNet}(r, z) \in \mathbb{R}^K. \quad (7)$$

The two embeddings are combined via element-wise multiplication, and the result is passed to a shallow *head network* that produces the predicted flux:

$$\hat{\psi}(r, z; \mathbf{d}) = \text{HeadNet}_{\psi}(\mathbf{t}(r, z) \odot \mathbf{b}) \quad (8)$$

This formulation modifies the original DeepONet, which uses a dot product between branch and trunk outputs, by replacing it with an element-wise product followed by a regression head. The branch network thereby acts as a *conditioner*: it encodes the current plasma scenario, captured in the magnetic measurements \mathbf{d} , and modulates the spatial basis functions provided by the trunk. All three sub-networks are implemented as single-layer MLPs with the custom activation function described below.

3) *Activation Function*: Because the physics-informed losses (introduced below) require first- and second-order partial derivatives of $\hat{\psi}$ with respect to (r, z) , and these derivatives must themselves be differentiated through the optimiser during training, a third-order differentiable activation function is necessary. The Swish function [34] satisfies this requirement and is infinitely differentiable:

$$\text{Swish}_{\beta}(x) = x \sigma(\beta x) = \frac{x}{1 + e^{-\beta x}}, \quad (9)$$

$$\frac{d}{dx} \text{Swish}_{\beta}(x) = \sigma(\beta x) + \beta x \sigma(\beta x) [1 - \sigma(\beta x)]. \quad (10)$$

where β is a vector of trainable per-unit parameters that controls the sharpness of the activation. This trainable parametrization allows a single-layer network to achieve high nonlinear expressivity without increasing depth, which is critical for inference speed.

4) *Physics-Informed Regularization*: Three loss terms are propagated jointly through the network during training. Using Eqs. (3)–(4), the predicted field components \hat{B}_r , \hat{B}_z , and \hat{j} are obtained by automatic differentiation of $\hat{\psi}$ with respect to (r, z) . The individual loss terms are:

$$\mathcal{L}_{\psi} = \frac{1}{N_c} \sum_{i=1}^{N_c} |\hat{\psi}(r_i, z_i) - \psi_{\text{LIUQE}}(r_i, z_i)|^p \quad (11)$$

$$\mathcal{L}_B = \frac{1}{N_c} \sum_{i=1}^{N_c} |\hat{\mathbf{B}}(r_i, z_i) - \mathbf{B}_{\text{LIUQE}}|^p \quad (12)$$

$$\mathcal{L}_j = \frac{1}{N_c} \sum_{i=1}^{N_c} |\hat{j}(r_i, z_i) - j_{\text{LIUQE}}|^p \quad (13)$$

where $p \in \{1, 2\}$ (both ℓ_1 and ℓ_2 norms were found to work in practice), N_c is the number of collocation points per batch, and all targets are taken directly from LIUQE. The total training loss is the weighted sum:

$$\mathcal{L} = \lambda_{\psi} \mathcal{L}_{\psi} + \lambda_B \mathcal{L}_B + \lambda_j \mathcal{L}_j. \quad (14)$$

The weights λ_{ψ} and λ_B , with $\lambda_{\psi} = 10 \lambda_B$, are kept constant throughout training, giving higher importance to direct flux accuracy. The weight λ_j is initialized at a relatively large value and decayed exponentially during training: the current-density loss accelerates convergence in the early stages, but is tapered toward the end because j is not a control target, and also to avoid overfitting to the core current-density profiles,

which are ill-posed with respect to the boundary magnetic measurements and vary across scenarios.

5) *Collocation Point Sampling*: During training, query points (r_i, z_i) are drawn from a non-uniform distribution that concentrates samples near the LCFS. This importance sampling strategy serves two purposes. First, the LCFS and its neighbourhood are the most control-relevant region of the domain, since virtually all shape control quantities — gap distances, X-point positions, flux-surface geometry — are derived from features of ψ near the plasma boundary. Second, because the model does not receive plasma pressure or current profiles as inputs — consistent with standard practice in real-time equilibrium reconstruction — sampling fewer points in the plasma core reduces the influence of profile-dependent reconstruction errors on the training loss. In the absence of profile information, the network is expected to learn the most probable core profile consistent with the measurement-conditioned boundary solution.

6) *Training Procedure*: The model is trained using the Adam optimiser with a batch size of 256 and a learning rate that decays logarithmically from 5×10^{-3} to 5×10^{-5} over 50 epochs. The branch/trunk split architecture was found to converge significantly faster and to achieve the same reconstruction accuracy with fewer total trainable parameters compared to a monolithic fully-connected network with identical input/output dimensions. Training and validation loss curves for \mathcal{L}_ψ and \mathcal{L}_B are shown in Fig. 2.

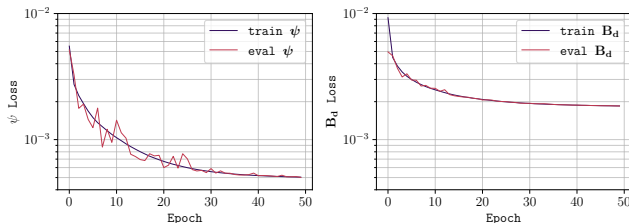


Fig. 2. Training and validation loss curves for the flux loss \mathcal{L}_ψ (left) and the magnetic-field loss \mathcal{L}_B (right).

D. Implementation on the Plasma Control System

Deployment on the TCV plasma control system (PCS) [35] required the network to be compiled to efficient native code compatible with the real-time control infrastructure. The model was implemented as a MATLAB function (r2019a) with code-generation compatibility, allowing the MATLAB/Simulink engine to compile it into efficient C code. This approach guarantees modularity and interoperability with the other control system submodules.

Magnetic field components B_r and B_z are required at run time and are computed by performing a single back-propagation step through the trunk-network path, exploiting the same automatic differentiation mechanism used during training. Profiling of the compiled code revealed that approximately 80% of the real-time execution time was consumed by the evaluation of exponentials in the Swish activation function. A key optimization was to cache the exponential

TABLE I

DEPLOYED VERSIONS AND MEASURED RECONSTRUCTION TIME

Vers.	Emb. size	Trunk	Branch	Head	t_r (μs)
Small	32	32	48	48	78 ± 5
Turbo	16	16	32	32	20 ± 1

values computed during the forward pass and reuse them during the backward pass for B_r , B_z computation: because the forward and backward activations share the same sigmoid (see Eq. 10), this avoids redundant exponential evaluations and reduces the total inference time by nearly a factor of two. A further optimization — caching and reusing the trunk embedding across time steps when the set of control points does not change within a shot — was identified but deliberately not implemented, in order to preserve the modularity of the approach and allow dynamic control point selection at run time.

The module was deployed as a submodule of the full control scheme on a reserved CPU core (Intel i9) of the TCV control server, where it can run in parallel with the active control system during shots, allowing real-time speed characterization without interfering with machine operations. Two network variants were characterized, as summarized in Table I. Both variants operate comfortably within the 100 μs budget required for 10 kHz control.

III. RESULTS

A. Network Reconstruction Capabilities

Figure 3 shows validation-set reconstructions for four plasma configurations (see caption for column layout).

The flux ψ achieves the best accuracy, consistent with its dominant weight ($\lambda_\psi = 10 \lambda_B$) in the training loss. B_r and B_z are accurate across most of the domain, with somewhat higher errors near the vessel corners — regions outside the plasma vessel not covered by training collocation points. j shows the largest errors, as expected: it is not a primary control objective, its reconstruction from boundary measurements alone is ill-posed, and λ_j is deliberately decayed to avoid overfitting core profiles. The single-null row achieves the best accuracy across all fields, reflecting its predominance in the training set. The double-null row shows good accuracy near the boundary but higher core errors, as the network must infer the core current-density profile from measurements rather than receiving it as input. The remaining configurations confirm good generalization to advanced shapes and a wide range of vertical positions.

B. Comparison with LIUQE-RT and LIH

The reconstruction accuracy of the PINO surrogate is compared against LIUQE-RT and LIH, using the offline LIUQE solution as the ground truth. Figure 4 shows the average and maximum absolute errors across 25 reference control points on the plasma boundary, as a function of time within the discharge (from 0.2 s to 1.6 s), for the flux ψ and the total poloidal magnetic field magnitude $\sqrt{B_r^2 + B_z^2}$.

The PINO trace is generated in real time on the TCV PCS during the shot, while the LIUQE-RT and LIH traces are

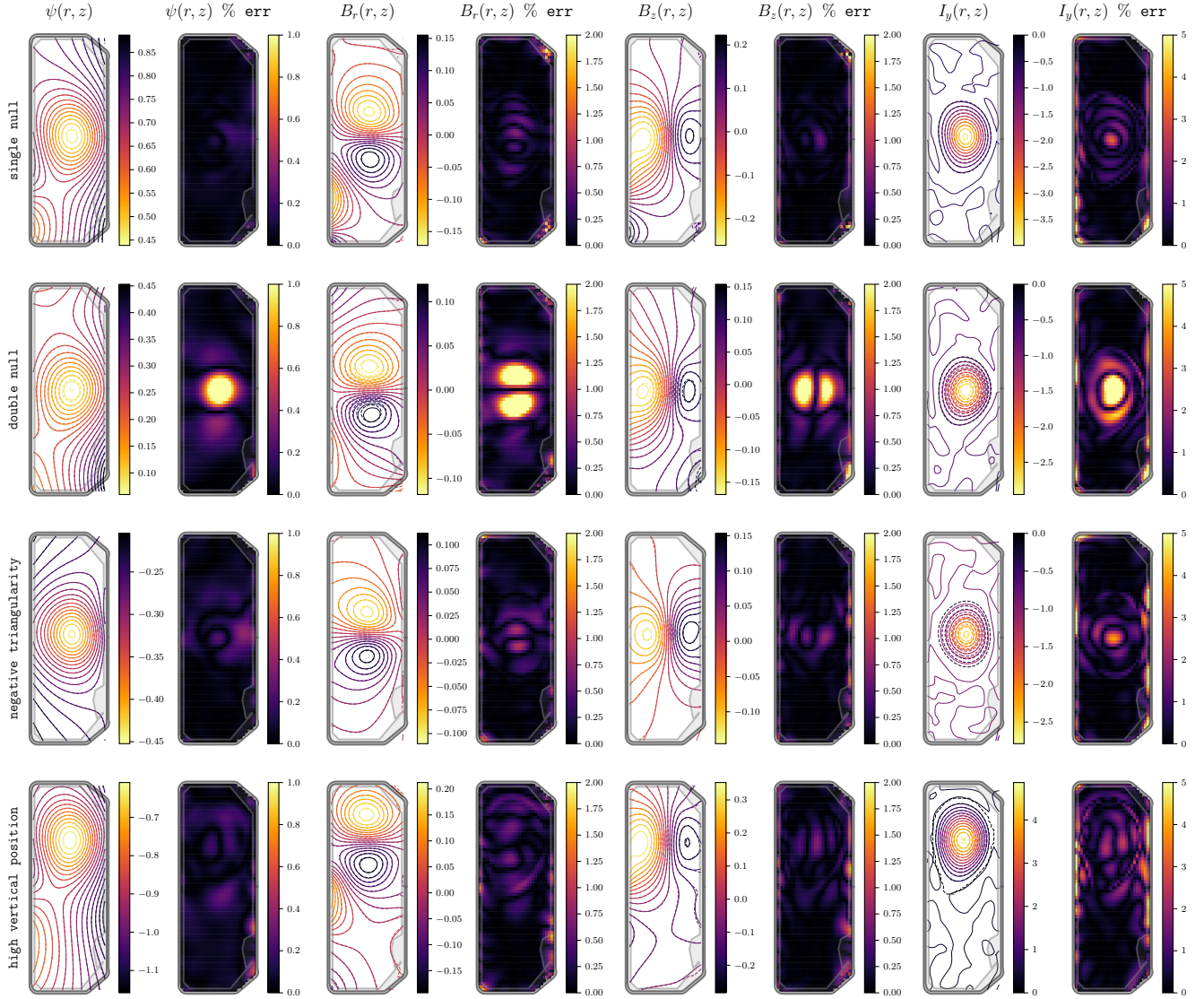


Fig. 3. Reconstruction examples from the validation set for 4 distinct plasma configurations (rows). Collocation points are selected to be the entire regular grid to evaluate contours. The eight columns show, from left to right: predicted vs. ground-truth poloidal flux contours (PINO: solid, LIUQE: dotted), absolute percentage error on ψ (saturated at 1%), B_r contours, percentage error on B_r (saturated at 2%), B_z contours, percentage error on B_z (saturated at 2%), toroidal current density j contours, and percentage error on j (saturated at 5%). Row 1: standard single-null. Row 2: double-null. Row 3: Negative triangularity. Row 4: High vertical position.

computed offline in post-processing for the same shot. LIH, as expected, is the least accurate of the three observers: its error is the largest and remains relatively constant throughout the discharge, consistent with its nature as a zero-iteration first guess. Nevertheless, even LIH produces errors that remain within a range considered feasible for control purposes. The PINO surrogate and LIUQE-RT perform very similarly, with both observers achieving errors that remain mostly at or below the 10^{-3} [Wb, T] level across both quantities. Notably, the PINO surrogate is substantially more accurate than LIUQE-RT for the flux ψ during the first half of the discharge. Averaged across multiple previously unseen shots, the PINO achieves average errors of 1.09×10^{-3} Wb, 1.33×10^{-3} T, and 1.12×10^{-3} T for ψ , B_r , and B_z

respectively — compared to 6.55×10^{-3} Wb, 1.20×10^{-3} T, 9.75×10^{-4} T for LIUQE-RT, and 1.37×10^{-2} Wb, 9.11×10^{-3} T, 1.12×10^{-2} T for LIH. These residual errors are comparable to the calibration uncertainty of the magnetic sensors, indicating that the surrogate is operating near the measurement noise floor.

C. Closed-Loop Control Simulations

The closed-loop performance of the PINO surrogate as a shape-control observer is assessed in simulation using the FGE free-boundary equilibrium and transport solver [2], [36], thoroughly validated on TCV. Three controllers of increasing complexity are considered; in all cases solid lines correspond to the PINO surrogate and dashed lines to the

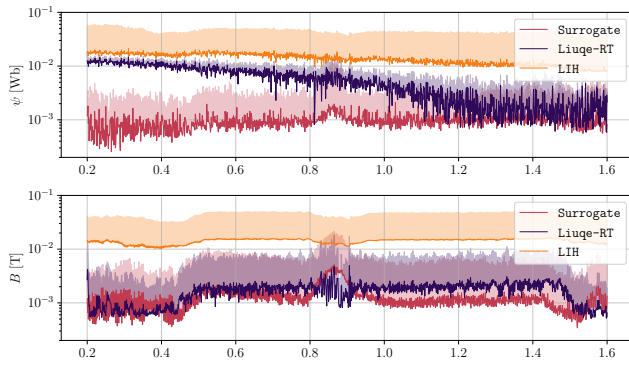


Fig. 4. Reconstruction error comparison across 25 reference control points on a representative shot, as a function of discharge time. In each panel, two lines are shown per observer: the temporal trace of the average error (lower) and maximum error (upper) across the 25 points. All errors are computed with respect to the offline LIUQE solution, taken as ground truth.

default observer.

PID gap-based controller. The first controller is the PID-based hybrid shape controller of [37], which tracks a set of gap distances on the plasma boundary, activated at $t = 0.6$ s with LIUQE-RT as the default observer. Figure 5 shows the shape control errors across the 10 control points (left) and the projected shape errors (right). Both observers produce essentially indistinguishable closed-loop behaviour: all error channels converge after activation, with the surrogate achieving marginally faster settling on some channels.

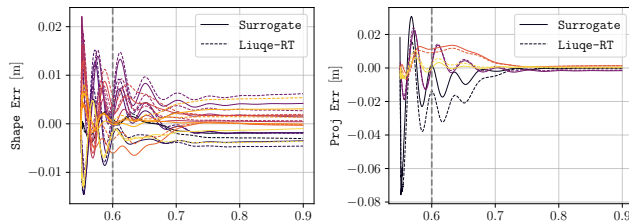


Fig. 5. Closed-loop simulation with the PID-based hybrid gap controller [37] (default observer: LIUQE-RT). Left: shape control errors on the plasma boundary across 10 control points. Right: projected shape control errors. The vertical gray dashed line marks controller activation at $t = 0.6$ s.

MPC isoflux-based controller. The second controller is a Model Predictive Controller [38] that tracks flux-surface targets rather than gap distances, using the same shot and activation time. The QP decision variable is the optimal control increment ΔU expressed in a SVD-reduced basis of the control space; Fig. 6 shows the flux-based shape errors (left) and the first six SVD components of the optimal ΔU [kA/s] (right). The controller activates at $t \approx 0.62$ s, delayed by Kalman filter convergence. Shape errors (left) are virtually identical to the PID case, as expected for the same shot and target. The optimal control increments (right) are also very similar between the two observers after the initial transient, confirming that the surrogate drives the MPC to the same control solution as LIUQE-RT.

FMag mixed controller. The third controller is an exper-

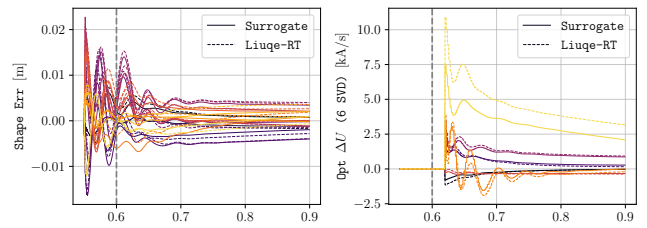


Fig. 6. Closed-loop simulation with the flux-based MPC controller [38] (default observer: LIUQE-RT). Left: flux-based shape control errors across 10 control points. Right: first six SVD components of the optimal control increment ΔU [kA/s]

imental mixed controller (FMag) that simultaneously regulates plasma current, radial and vertical position, and X-point location. This controller operates at 10 kHz, so the default observer is LIH rather than LIUQE-RT; the PINO surrogate replaces LIH only for the X-point observer, while position and plasma current observers are identical in both runs. Figure 7 shows the X-point position errors Δr (blue) and Δz (red) in cm (left) and the mixed control errors in arbitrary units (right). In both cases the controller successfully drives all channels to zero; X-point tracking and mixed errors are similarly tight for the surrogate and LIH, with no degradation from the observer substitution.

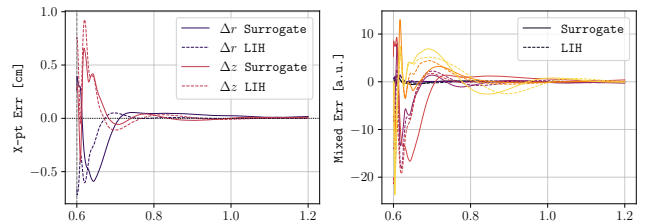


Fig. 7. Closed-loop simulation with the experimental FMag mixed controller operating at 10 kHz. Left: X-point position errors Δr (blue) and Δz (red) in cm. Right: mixed control errors in arbitrary units across controlled channels.

Across all three controllers the PINO surrogate produces closed-loop behavior that is essentially equivalent to the respective default observer, demonstrating that the surrogate is a viable drop-in replacement across a range of control architectures and bandwidths.

IV. CONCLUSIONS

We have presented a PINO surrogate for real-time plasma equilibrium reconstruction on TCV, targeting the 10 kHz bandwidth required for advanced shape control. Based on a modified DeepONet [22] with branch/trunk decomposition, it enforces physics-informed regularization via automatic differentiation using LIUQE-generated targets on ψ , B_r , B_z , and j .

Trained on around 10000 TCV shots and deployed on the TCV PCS, the surrogate achieves 20–80 μ s inference at 25 control points, well within the 100 μ s budget for 10 kHz operation. Offline and online validation demonstrated

accuracy comparable to or better than LIUQE-RT, and closed-loop FGE simulations [2] with three controllers of increasing complexity — a PID gap-based controller, a isoflux-based MPC, and a 10 kHz experimental mixed controller — confirmed essentially equivalent control performance in every case, establishing the viability of PINO-based equilibrium reconstruction as a practical real-time observer.

Two limitations remain. First, the absence of plasma profile inputs leads to higher reconstruction errors in the plasma core. Second, generalization to strongly out-of-distribution or completely new configurations is not guaranteed and should be verified before deploying the surrogate as the sole observer.

Natural extensions include *pre-shot fine-tuning* — a brief fine-tuning pass before the discharge to improve accuracy for demanding target shapes; adding plasma profile inputs to reduce core reconstruction errors; and the transition to a *predictive* role, forecasting plasma response to PF coil changes over a short horizon to enable model-based predictive control.

Real-time closed-loop testing on actual TCV shots, in which the PINO surrogate directly drives the shape controller in the PCS, is currently in preparation and will be the subject of a forthcoming contribution.

ACKNOWLEDGMENTS

This work has been carried out within the framework of the EUROfusion Consortium, funded by the European Union via the Euratom Research and Training Programme (Grant Agreement No 101052200 — EUROfusion). Views and opinions expressed are however those of the author(s) only and do not necessarily reflect those of the European Union or the European Commission. Neither the European Union nor the European Commission can be held responsible for them. This work was also partially funded by the Italian Ministry of University and Research (MUR) under the National Recovery and Resilience Plan (PNRR), funded by the European Union – NextGenerationEU.

REFERENCES

- [1] J.-M. Moret *et al.*, “Tokamak equilibrium reconstruction code liuqe and its real time implementation,” *Fusion Engineering and Design*, vol. 91, pp. 1–15, 2015.
- [2] F. Carpanese, “Development of free-boundary equilibrium and transport solvers for simulation and real-time interpretation of tokamak experiments,” Ph.D. dissertation, EPFL, Lausanne, 2021.
- [3] B. Duval *et al.*, “Experimental research on the tcv tokamak,” *Nuclear Fusion*, vol. 64, no. 11, p. 112023, Oct. 2024.
- [4] V. D. Shafranov, “Plasma Equilibrium in a Magnetic Field,” *Reviews of Plasma Physics*, vol. 2, p. 103, Jan. 1966.
- [5] H. Grad *et al.*, “Hydromagnetic equilibria and force-free fields,” *Journal of Nuclear Energy*, vol. 7, pp. 284–285, 1958.
- [6] J. Wai *et al.*, “Neural net modeling of equilibria in nstx-u,” *Nuclear Fusion*, vol. 62, no. 8, p. 086042, Jul. 2022.
- [7] L. L. Lao *et al.*, “Application of machine learning and artificial intelligence to extend efit equilibrium reconstruction,” *Plasma Physics and Controlled Fusion*, vol. 64, no. 7, p. 074001, Jun. 2022.
- [8] S. Madireddy *et al.*, “Efit-prime: Probabilistic and physics-constrained reduced-order neural network model for equilibrium reconstruction in diii-d,” *Physics of Plasmas*, vol. 31, no. 9, Sep. 2024.
- [9] J. Lu *et al.*, “Fast equilibrium reconstruction by deep learning on east tokamak,” *AIP Advances*, vol. 13, no. 7, Jul. 2023.
- [10] G. Zheng *et al.*, “Real-time equilibrium reconstruction by neural network based on hl-3 tokamak,” 2024.
- [11] —, “Efit-mini: An embedded, multi-task neural network-driven equilibrium inversion algorithm,” 2025.
- [12] Y. Liu *et al.*, “Surrogate models for plasma displacement and current in 3d perturbed magnetohydrodynamic equilibria in tokamaks,” *Nuclear Fusion*, vol. 62, no. 12, p. 126067, Nov. 2022.

- [13] B. Leard *et al.*, “Self-consistent equilibrium and transport simulations for nstx-u plasmas enhanced via machine learning surrogate models,” *Fusion Engineering and Design*, vol. 219, p. 115201, Oct. 2025.
- [14] S. Joung *et al.*, “Deep neural network grad-shafranov solver constrained with measured magnetic signals,” *Nuclear Fusion*, vol. 60, no. 1, p. 016034, Dec. 2019.
- [15] Z. Wang *et al.*, “Neural-network-based free-boundary equilibrium solver to enable fast scenario simulations,” *IEEE Transactions on Plasma Science*, vol. 52, no. 9, pp. 4147–4153, 2024.
- [16] F. Fiorenza *et al.*, “Caronte: a physics-informed extreme learning machine-based algorithm for plasma boundary reconstruction in magnetically confined fusion devices,” 2025.
- [17] M. S. Stokolesov *et al.*, “Reconstructing the plasma boundary with a reduced set of diagnostics,” 2025.
- [18] V. Tribaldos *et al.*, “Neural network tool for rapid recovery of plasma topology,” *Review of Scientific Instruments*, vol. 68, no. 1, 01 1997.
- [19] S. Joung *et al.*, “Gs-deepnet: mastering tokamak plasma equilibria with deep neural networks and the grad-shafranov equation,” *Scientific Reports*, vol. 13, no. 1, Sep. 2023.
- [20] J. McClenaghan *et al.*, “Augmenting machine learning of grad-shafranov equilibrium reconstruction with green’s functions,” *Physics of Plasmas*, vol. 31, no. 8, Aug. 2024.
- [21] M. Bonotto *et al.*, “Reconstruction of plasma equilibrium and separatrix using convolutional physics-informed neural operator,” *Fusion Engineering and Design*, vol. 200, p. 114193, Mar. 2024.
- [22] L. Lu *et al.*, “Learning nonlinear operators via deepnet based on the universal approximation theorem of operators,” *Nature Machine Intelligence*, vol. 3, no. 3, pp. 218–229, Mar. 2021.
- [23] T. Chen *et al.*, “Universal approximation to nonlinear operators by neural networks with arbitrary activation functions and its application to dynamical systems,” *IEEE Transactions on Neural Networks*, vol. 6, no. 4, p. 911–917, Jul. 1995.
- [24] S. Ding *et al.*, “Physics-informed neural operator learning for nonlinear grad-shafranov equation,” 2025.
- [25] F. N. Rizqan *et al.*, “Evaluation and verification of physics-informed neural models of the grad-shafranov equation,” 2025.
- [26] D. A. Kaltsas *et al.*, “Neural network tokamak equilibria with incompressible flows,” *Physics of Plasmas*, vol. 29, no. 2, Feb. 2022.
- [27] C. M. Bishop *et al.*, “Real-time control of a tokamak plasma using neural networks,” *Neural Computation*, vol. 7, no. 1, pp. 206–217, 1995.
- [28] Y.-M. Jeon *et al.*, “Newly developed double neural network concept for reliable fast plasma position control,” *Review of Scientific Instruments*, vol. 72, no. 1, pp. 513–516, Jan. 2001.
- [29] A. A. Prokhorov *et al.*, “The plasma shape control system in the tokamak with the artificial neural network as a plasma equilibrium reconstruction algorithm,” *IFAC-PapersOnLine*, vol. 53, no. 2, pp. 857–862, 2020.
- [30] J. Degraeve *et al.*, “Magnetic control of tokamak plasmas through deep reinforcement learning,” *Nature*, vol. 602, no. 7897, pp. 414–419, Feb. 2022.
- [31] G. F. Subbotin *et al.*, “Reconstruction-free magnetic control of diii-d plasma with deep reinforcement learning,” 2025.
- [32] N. Wu *et al.*, “High-fidelity data-driven dynamics model for reinforcement learning-based control in hl-3 tokamak,” 2025.
- [33] A. Dave *et al.*, “Fpga-accelerated real-time beam emission spectroscopy diagnostics at diii-d using the slac neural network library for ml inference,” 2025.
- [34] P. Ramachandran *et al.*, “Searching for activation functions,” 2017.
- [35] C. Galperti *et al.*, “Overview of the tcv digital real-time plasma control system and its applications,” *Fusion Engineering and Design*, vol. 208, p. 114640, Nov. 2024.
- [36] C. Heiß *et al.*, “Fge: A fast free-boundary grad-shafranov evolutive solver,” 2025.
- [37] H. Anand *et al.*, “A novel plasma position and shape controller for advanced configuration development on the tcv tokamak,” *Nuclear Fusion*, vol. 57, no. 12, p. 126026, Sep. 2017.
- [38] A. Mele *et al.*, “First experimental demonstration of plasma shape control in a tokamak through model predictive control,” 2025.